crystals

MDPI

Article

First Principle Analysis on Elastic and Mechanical Behavior of High-Pressure Hexagonal $MgZn_2$ Phase

Chuncai Xiao [1], Baiyuan Yang [2], Zhangli Lai [2], Xianshi Zeng [2], Zhiquan Chen [2], Yunzhi Zhou [2] and Donglan Wu [2,*]

[1] School of Mechanical and Electrical Engineering, Xinyu University, Xinyu 338004, China; xiaochuncai123@yeah.net
[2] School of Mathematical Sciences and Physics, Jinggangshan University, Ji'an 343009, China; yangabai@163.com (B.Y.); 15979627768@163.com (Z.L.); zengxueliang@163.com (X.Z.); chenzhiquanji@126.com (Z.C.); 9920060050@jgsu.edu.cn (Y.Z.)
* Correspondence: wudonglan1216@sina.com

Abstract: There is a paucity of previous related studies exploring hexagonal $MgZn_2$ in high-pressure environments. This study systematically analyzes the mechanical behavior of $MgZn_2$ hexagonal alloys under high-pressure conditions using first principle calculations, bridging the gap in research in this area in the field. The results reveal that, with increasing pressure, the crystallite spacing (a/a_0, c/c_0) and ratio of volumes (V/V_0) decrease significantly, indicating the structural condensation of the material under high pressure. Elastic constant analysis showed a notable enhancement in all constants, except for C_{13}. Among them, C_{11} increased from 87.399 GPa to 311.45 GPa, and C_{33} increased from 135.279 GPa to 341.739 GPa, showing a faster growth rate, suggesting improved tensile strength in the material along the tensile direction. Mechanical stability assessments confirmed that the alloy remains stable over the 0 to 30 GPa pressure range. Further material characterization indicated that Poisson's ratio remained above 0.26 at pressures from 0 to 30 GPa, suggesting excellent ductility and agreeing with the ratio of the shear modulus to the bulk modulus. As the pressure increases, both the hardness and sound velocity of $MgZn_2$ increase, while the degree of anisotropy decreases. The present work gives important insights on the mechanical behavior of $MgZn_2$ under high pressure, contributing to its application and property optimization.

Keywords: first principle calculations; mechanical properties; hexagonal $MgZn_2$; high pressure; elastic constants

check for updates

Citation: Xiao, C.; Yang, B.; Lai, Z.; Zeng, X.; Chen, Z.; Zhou, Y.; Wu, D. First Principle Analysis on Elastic and Mechanical Behavior of High-Pressure Hexagonal $MgZn_2$ Phase. *Crystals* **2024**, *14*, 1090. https://doi.org/10.3390/cryst14121090

Academic Editor: Catalin Popescu

Received: 15 November 2024
Revised: 9 December 2024
Accepted: 17 December 2024
Published: 18 December 2024

Copyright: © 2024 by the authors. Licensee MDPI, Basel, Switzerland. This article is an open access article distributed under the terms and conditions of the Creative Commons Attribution (CC BY) license (https://creativecommons.org/licenses/by/4.0/).

1. Introduction

In contemporary science and engineering, magnesium alloys have gained considerable attention due to the combination of a high specific strength, low density and outstanding resistancy to corrosion [1]. These properties make them increasingly important in industries such as aerospace, the automotive industry and electronics, where lightweight materials are in high demand [2,3]. The growing need for such materials has driven the research and development of magnesium alloys, making them a key factor in advancing these industries [4,5]. However, despite their many advantages, magnesium alloys still face challenges related to performance at high temperatures and in harsh environments, particularly concerning their strength and corrosion resistance, which limits their broader application [6–8].

$MgZn_2$, an important intermetallic compound in magnesium alloys, performs a crucial function in improving the microstructures and mechanical properties of alloys [9,10]. The structure of $MgZn_2$ is hexagonal close-packed (hcp), which endows it with excellent mechanical properties [11]. Additionally, $MgZn_2$ can contribute to solid solution strengthening within the alloy. Studies have also shown that $MgZn_2$ can inhibit the corrosion behavior of magnesium alloys, improving their reliability in harsh environments [12,13]. Compared with similar compounds, $MgZn_2$ has prominent advantages. It has a good

lattice matching degree with the magnesium matrix. When incorporated into alloys, it can achieve good strengthening effects and avoid problems such as internal stresses and defects derived from a lattice mismatch. However, it also has shortcomings. When the temperature exceeds a specific value under high-temperature conditions, its antioxidant performance is relatively poor, and loose oxide layers are prone to form on its surface, resulting in a decline in its performance. Andrae et al. [14] studied the electronic structure of the intermetallic compound $MgZn_2$ through first principle-based calculations using the density functional theory of Kohn-Sham where different exchange–correlation energetic functionals had been used to optimize the crystalline structure, showing that cell and mass densities obtained using the density functional parameterization method of Perdew, Burke and Ernzerhof (PBE) were closest to the results of the experiment and better than those of PBEsol and other functionals. The results showed that the cell parameters and mass densities obtained by the Perdew, Burke and Ernzerhof (PBE) density function parameterized method were closest to the experimental values, which were better than those of the PBEsol functionals, and the electronic structures were analyzed for energy bands, the electronic density and the density of state dimensions. Wu et al. [15] studied the structural, electrical and elastic characteristics of the $MgZn_2$ phase and the typical close-packed hexagonal structure of Mg-Sc-Zn alloys with the help of density functional theory (DFT)-based first principle calculations. The lattice constants calculated agreed well with the experimental results, and the negative energies of aggregation and the enthalpy of production between the two phases indicated the structural stability. The series moduli were derived from polycrystalline assemblies, the ductility, plasticity and elastic anisotropy were analyzed, and the density of states (DOS) and density of charge distributions were calculated to reveal intrinsic mechanisms.

Although numerous studies have examined the effect of $MgZn_2$ upon magnesium alloy properties, in-depth investigations of its behavior and mechanical properties under varying pressure and temperature conditions remain limited. Therefore, calculating the modulus of elasticity and other properties of $MgZn_2$ using first principle methods will provide a more comprehensive understanding of its behavior under different environmental conditions. This, in turn, will offer a new theoretical foundation for the optimal design of magnesium alloys.

This study systematically explores the mechanical characteristics and elastic constants of $MgZn_2$ at different pressures, focusing on characteristics such as Young's and the shear and bulk modulus. In addition to providing a deeper appreciation of how $MgZn_2$ plays a role in magnesium alloys, the results will guide future research and practical applications, ultimately strengthening the basis for its use in alloyed magnesium in a wider range of industry sectors.

2. Calculation Details

Here, the high-pressure elastic constants of $MgZn_2$ alloys were investigated by applying the Generalised Gradient Approximation (GGA) method of Perdew–Burke–Ernzerhof (PBE) [16] as part of the density functional theory (DFT) [17,18] implemented in the Cambridge Serialised Total energy package (CASTEP) [19–21] code.The BFGS (Broyden–Fletcher–Goldfarb–Shanno) [22] algorithm was used to perform the atomic position and lattice parameter optimization, ensuring convergence criteria were met: a total energy deviation below 1.0×10^{-5} eV/atom, a maximal ion force below 0.03 eV/Å, a pressure deviation below 0.05 GPa and a maximal displacement of atoms below 1.0×10^{-3} Å. To model ion–electron interactions, the ultrasoft pseudopotential (USPP) [23] was employed. The configuration of valence electrons for magnesium (Mg) and zinc (Zn) was set to $2p^6 3s^2$ and $3d^{10} 4s^2$, respectively. A plane wave cut-off used 500 eV, and the criterion for convergence was 1.0×10^{-6} eV/atom. The Brillouin zone sampling was performed with a grid of $6 \times 6 \times 4$ k points using the Monkhorst–Pack scheme [24].

Prior to the elastic constant calculation, a full relaxation of the volume, shape and internal atomic positions of the $MgZn_2$ intermetallic compound at the given pressure was performed. Figure 1 depicts the architecture of hexagonal $MgZn_2$, which has a C14 Laves

structure [25] that is typical of metal and rare gas alloys [26]. With lattice parameters of a = 5.157 Å and c = 8.373 Å, the space group is P63/mmc (No. 194). The atomic configuration consists of four magnesium (Mg) atoms at the 4f position (0.333, 0.667, 0.75/−0.25) and eight zinc (Zn) atoms in the 2a (0, 0, 0) and 6h (0.1704/0.3407, 0.3407/0.1704, 0.75) positions in every second layer of magnesium atoms.

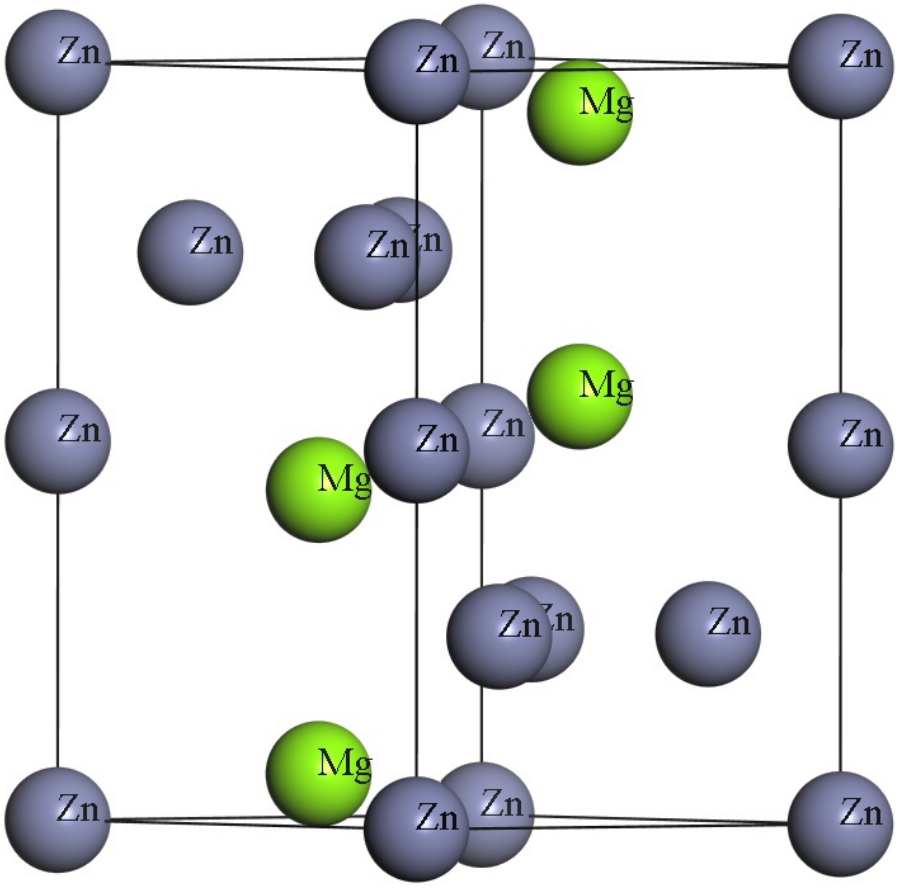


Figure 1. Hexagonal $MgZn_2$ unit cell structure.

In this study, the six independent constants of elasticity of a single crystal, C_{11}, C_{12}, C_{13}, C_{33},C_{44} and C_{66}, were calculated using a method based on strain–stress relationships from single cells optimized at different pressures. Elastic constants are the derivatives of the first-order stress in relation to the tensor of the strain. By applying six finite deformations to the lattice, the tensor of elasticity was derived from the relationship between the strain and stress [27]. Additionally, ion relaxation was considered in calculating the elastic tensor for rigid atoms. The ionic contribution was derived using the inverse Hessian of ionic matrices and multiplication by the inner strain tensor.

3. Results and Discussion

3.1. High-Pressure Structure Characteristics

The geometrical optimization of the $MgZn_2$ alloy was performed, and the optimizations of the lattice parameters obtained were a = 5.179Å and c = 8.602Å. These are consistent with previous studies. T. Ohba et al. [28] found that a = 5.233Å and c = 8.566Å; Mao et al. [29] reported that a = 5.23Å and c = 8.47Å; and Zheng et al. [30], using first principle calculations, determined that a = 5.1908Å and c = 8.6251Å. The results from this study agreed well with these experimentally and theoretically determined values, confirming the validity of using the calculation method.

We calculated the total energy E as a function of the lattice unit cell volume V and performed precise fitting using the Birch–Murnaghan Equation of State (EOS) [31]. The energy–volume relationship ($E - V$ curve) is presented in Figure 2. By employing the Birch–Murnaghan EOS, the relationship between the energy E and volume V was accurately predicted, allowing for the determination of the bulk modulus B_0 and its pressure derivative B_0'. The Birch–Murnaghan Equation of State is given as Equation (1) [32].

$$E(V) = E_0 + \frac{9}{16} V_0 B_0 \left\{ \left[\left(\frac{V_0}{V} \right)^{\frac{2}{3}} - 1 \right]^3 B_0' + \left[\left(\frac{V_0}{V} \right)^{\frac{2}{3}} - 1 \right]^2 \left(6 - 4 \left(\frac{V_0}{V} \right)^{\frac{2}{3}} \right) \right\} \quad (1)$$

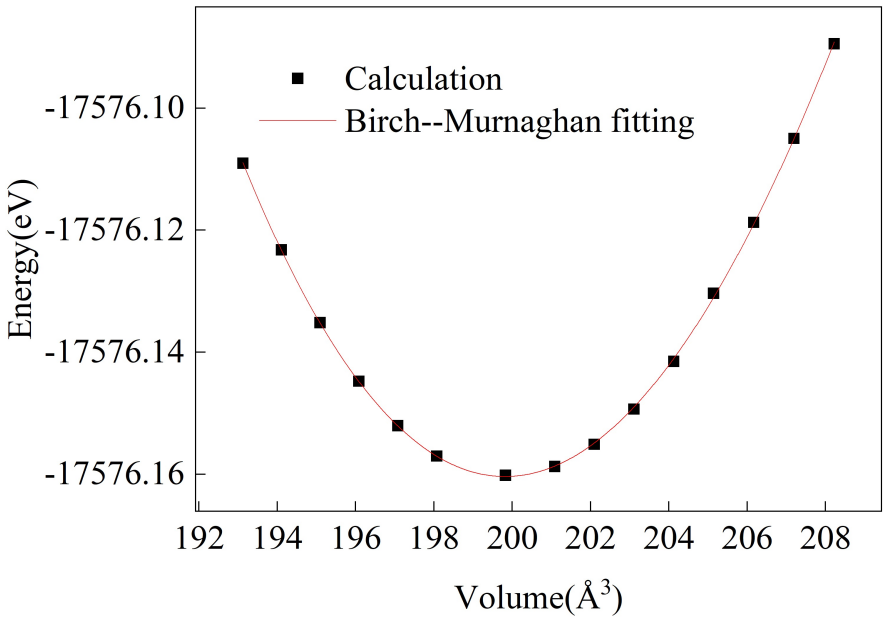


Figure 2. The fluctuation curve of the predicted total energy as a function of the $MgZn_2$ conventional cell volume.

The fitting results show that when the volume V is equal to the reference volume V_0 = 200.213Å^3, the total energy reaches its minimum at E_t = −17576.164 eV, indicating the equilibrium state. The corresponding lattice parameters are a = b = 5.179Å and c = 8.621Å, with a calculated bulk modulus of B_0 = 60.256 GPa.

Structural optimization was also carried out on $MgZn_2$ over a 0–30 GPa pressure range, further investigating the pressure dependence of the parameters. The variation with the pressure of the lattice parameters a/a_0 and c/c_0 and the volume V/V_0 is shown in Figure 3. The results indicate that both the a/a_0 and c/c_0 ratios gradually decrease with an increase in pressure, mainly due to compression of atomic spacing in the crystal under applied pressure.

The polynomial fitting of a/a_0, c/c_0 and V/V_0 to pressure values resulted in an equation describing the relationships between them, as shown in Equation (2). The constant term in the equation is close to one, indicating a good fit.

$$\begin{aligned} a/a_0 &= 0.9999 - 4.5600 \times 10^{-3} P + 9.99718 \times 10^{-5} P^2 - 1.18061 \times 10^{-6} P^3 \\ c/c_0 &= 0.99989 - 5.1000 \times 10^{-3} P + 1.13632 \times 10^{-4} P^2 - 1.32763 \times 10^{-6} P^3 \\ V/V_0 &= 0.99962 - 1.404 \times 10^{-3} P + 3.42579 \times 10^{-4} P^2 - 4.15028 \times 10^{-6} P^3 \end{aligned} \quad (2)$$

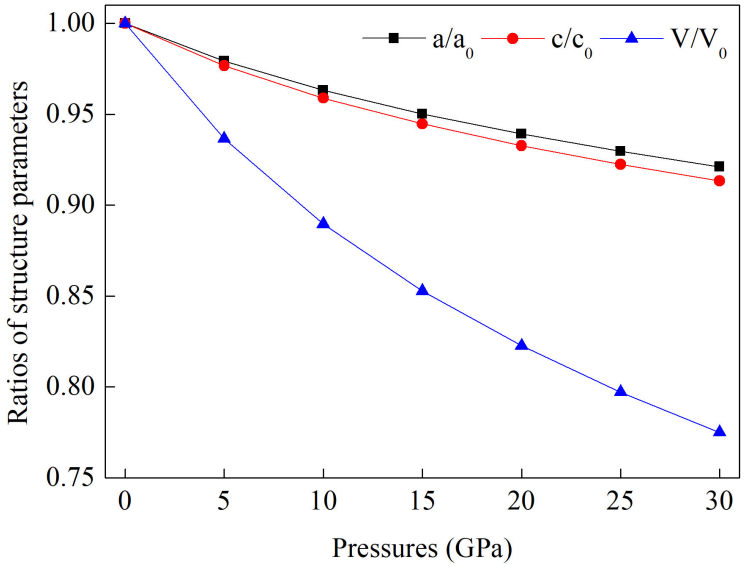


Figure 3. Variation in structural parameter ratios of a/a_0, c/c_0 and V/V_0 depending on pressure for $MgZn_2$.

3.2. Elastic Constants Under Pressure

The elastic constants of $MgZn_2$ were systematically analyzed to investigate the relationship between stress and strain in anisotropic media.

The hexagonal crystal $MgZn_2$ has independent constants of elasticity: C_{11}, C_{12}, C_{13}, C_{33} and C_{44}, with $C_{66} = (C_{11} - C_{12})/2$ used to calculate the shear strength. Specifically, C_{11} and C_{33} describe the strain response to tensile stresses applied across [100] and [001] crystal axes, respectively, while C_{44} and C_{66} reflect the shear resistance under shear stresses. C_{12} and C_{13} are associated with elastic deformation. It was found that C_{13} varied irregularly in the range of 0–30 GPa with the pressure, although overall the trend is upward. This may be caused by the fact that under pressure, the crystal structure of $MgZn_2$ becomes complex, with diverse interatomic interactions and mixed types of chemical bonding, uneven lattice distortion and stress distribution, varying changes in different crystallographic orientations and surfaces, and a localized stress concentration affecting atomic rearrangement. However, on the whole, the crystal structure tends to be more compact and stable with an increase in pressure, and the interatomic interactions are continuously enhanced, which makes C_{13} show an overall rising trend. In contrast, the remaining constants of elasticity increased monotonically in relation to the pressure. Notably, C_{11} and C_{33} exhibited a faster rate of increase under tensile stress, suggesting that the enhanced tensile resistance of $MgZn_2$ under high pressure may be linked to the increased compactness of its crystal structure. However, the slower rate of increase for C_{44} and C_{66} indicates that the material's shear resistance under shear stress is more limited, implying that the shear deformation capacity of the crystals is constrained at high pressures. The conditions for hexagonal crystal mechanical stability in isotropic pressure conditions are given by Equation (2) [33,34].

$$\tilde{C}_{44} > 0, \quad \tilde{C}_{11} - |\tilde{C}_{12}| > 0, \quad \tilde{C}_{33}(\tilde{C}_{11} + \tilde{C}_{12}) - 2\tilde{C}_{13}^2 > 0 \tag{3}$$

with $\tilde{C}_{ii} = C_{ii} - P$ $(i = 1, 3, 4)$, $\tilde{C}_{12} = C_{12} + P$ and $\tilde{C}_{13} = C_{13} + P$. The different criterion relationships relate to the differing deformation of hydrostatic pressure crystals, $\tilde{C}_{44}$ and $\tilde{C}_{66}$ reflect shearing deformations in the hydrostatically pressurized crystal cell and the values of $\tilde{C}_{11} - \tilde{C}_{12}$ reflect the expansion of the crystal in the major axis direction as well as the crystal cell contraction in the direction perpendicular to the principal axis. The values of $\tilde{C}_{33}(\tilde{C}_{11} + \tilde{C}_{12}) - 2\tilde{C}_{13}^2$ reflect the expansion of cells along the major axis and the contraction along the vertical major axis. The deformation of the $MgZn_2$ alloy under hydrostatic pressure was analyzed in relation to the pressure, and the correlation between different criteria and the crystal deformation was explored. The elastic constants of $MgZn_2$

under various pressures are given in Table 1. It was found that the expansion along the principal axis was closely linked to the contraction in the perpendicular direction, which collectively affected the overall deformation characteristics of the material. The volumetric deformation values indicate the volume change under different pressures. The evaluation results for the pressure range of 0 to 30 GPa in terms of the mechanical stability show that $MgZn_2$ meets the mechanical criterion and remains stable in this range.

Table 1. Constants of elasticity for various pressures of $MgZn_2$ (in GPa).

Pressure	C_{11}	C_{12}	C_{13}	C_{33}	C_{44}	C_{66}
0	87.399	78.111	18.189	135.279	22.816	4.644
5	113.183	86.850	17.019	157.669	31.074	13.166
10	151.391	106.451	41.163	208.729	37.965	22.470
15	198.445	133.180	86.579	283.226	44.174	32.633
20	246.002	157.498	74.943	273.643	50.638	44.252
25	280.553	168.986	104.822	333.947	56.508	55.784
30	311.450	176.873	98.172	341.739	63.360	67.289

3.3. Modulus of Elasticity and Compressive Mechanical Properties

The macromechanical parameters of the $MgZn_2$ alloy, including shear, Young's and bulk moduli with Poisson's ratio, were analyzed in this study. These properties give us an important indication of macromechanical characteristics in the crystal. The Reuss and Voigt approximations were used to calculate these parameters. The Reuss approximation assumes that stress is uniformly distributed within the polycrystalline material, providing the lower limit for shear and bulk moduli. In contrast, Voigt approximation assumes uniform strain distribution across the polycrystalline structure, yielding the upper limit. To obtain a more accurate estimate, Hill proposed an approximation called the Voigt–Reuss–Hill [35], which averages the results of Reuss and Voigt approximations.

In this method, the crystal bulk and shear moduli are calculated using the average of the Voigt bulk modulus (B_V), Reuss bulk modulus (B_R), Voigt shear modulus (G_V) and Reuss shear modulus (G_R). The definitions of B_V and B_R and G_V and G_R in the hexagonal crystallographic system are given in Equation (4) [36,37].

$$\begin{aligned} B_V &= \frac{2C_{11}+2C_{12}+4C_{13}+C_{33}}{9} \\ G_V &= \frac{C_{11}+C_{12}-4C_{13}+2C_{33}+12C_{44}+12C_{66}}{30} \\ B_R &= \frac{(C_{11}+C_{12})C_{33}-2C_{13}^2}{C_{11}+C_{12}-4C_{13}+2C_{33}} \\ G_R &= \frac{5\left[(C_{11}+C_{12})C_{33}-2C_{13}^2\right]C_{44}C_{66}}{6B_VC_{44}C_{66}+2\left[(C_{11}+C_{12})C_{33}-2C_{13}^2\right](C_{44}+C_{66})} \end{aligned} \tag{4}$$

with $C_{66} = (C_{11} - C_{12})/2$. After calculating B_V and G_V using Voigt approximation and B_R and G_R using Reuss approximation, G for the shear modulus, B for the bulk modulus, E for Young's modulus and ν for Poisson's ratio were further calculated according to Equation (5) for different pressures of certain phases.

$$B = \frac{B_V + B_R}{2}, \quad G = \frac{G_V + G_R}{2}, \quad E = \frac{9BG}{3B + G}, \quad \nu = \frac{3B - 2G}{6B + 2G} \tag{5}$$

The relationship between the bulk modulus (B), shear modulus (G) and Young's modulus (E) of $MgZn_2$ intermetals and the pressure is shown in Figure 4. The modulus of shear (G) reflects the material's strength against shear deformations under stress, the modulus of bulk (B) characterizes the material's strength against volumetric deformations when stress is applied, and E measures the stiffness of the material, with higher values indicating stiffer material. Figure 4 shows all three moduli—B, G and E—increasing steadily with the pressure. This behavior is due to the high symmetricality of the hexagonal crystal

structure of $MgZn_2$. As the pressure increases, atomic relationships are altered within the lattice, resulting in an increase in these moduli.

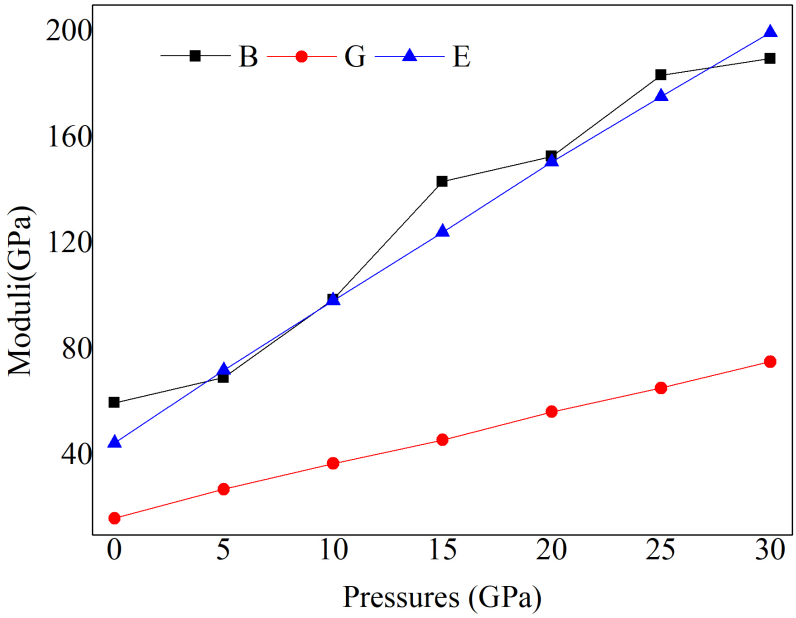


Figure 4. Bulk (B), shearing (G) and Young's (E) modulus for different pressures of $MgZn_2$.

We conducted a detailed analysis of Poisson's ratio (ν) and the ratio of the bulk to shear modulus (B/G)for $MgZn_2$ alloys to investigate their mechanical behavior. According to Frantsevich et al.'s rule [38], the material exhibits predominantly brittle behavior if the ratio of Poisson (ν) is under 0.26; conversely, it displays ductility when $\nu > 0.26$. Figure 5a shows the variation with the pressure of Poisson's ratio for $MgZn_2$. In a pressure range of 0–5 GPa, ν tends to decrease, reaching 0.327 at 5 GPa. Between 5 and 15 GPa, ν increases with the pressure, but it begins to decrease again when the pressure exceeds 15 GPa. Overall, Poisson's ratio for $MgZn_2$ remains greater than 0.26 throughout the 0–30 GPa range, indicative of the material's ductility. The relationship between B and G is strongly related to Pugh's rule for the brittleness and ductility of a material [39]: a greater B/G indicates greater ductility. The material can be considered ductile if $B/G > 1.75$. Figure 5b shows the variation in the B/G relationship with pressure for $MgZn_2$. The B/G value decreases in the 0–5 GPa range, reaching 2.552 at 5 GPa. It then increases with the pressure between 5 and 15 GPa, before decreasing again when the pressure exceeds 15 GPa. Overall, the B/G ratio of $MgZn_2$ remains above 1.75 across the range of 0–30 GPa, confirming its ductility, consistent with the trend observed in Poisson's ratio. As a next step, the ductility can be improved by alloying. Adding elements with good ductility, such as aluminum and copper, into the crystal lattice can change the bonding characteristics, increase the slip system, help the dislocation movement and regulate the direction and strength of the chemical bond to enhance the deformation capacity. At the same time, of thermo-mechanical treatment can be used to refine the grain, increase the grain boundaries to hinder crack expansion and promote plastic deformation, thereby improving the ductility.

The Cauchy pressure on the (100) face is defined as $C_{13} - C_{44}$ for a hexagonal crystal structure and is defined on the (001) face as $C_{12} - C_{66}$. According to Pettifor's rule [40], a more positive Cauchy pressure means a higher metallic bond count in the material, enhancing its toughness, while a more negative Cauchy pressure indicates greater covalent bonding, leading to brittleness. Figure 6 illustrates the Cauchy pressure of $MgZn_2$ at different pressures. Starting from 0 GPa, $C_{12} - C_{66}$ increases with the pressure, reaching a maximum around 25 GPa, before slightly decreasing. Overall, $C_{12} - C_{66}$ increases smoothly with the pressure and remains above 75 GPa throughout the 0–30 GPa range. In contrast, the initial values of $C_{13} - C_{44}$ are close to zero at 0 GPa, become negative at 5 GPa, then

gradually rise to positive values, with fluctuations observed at various pressures. The values do not show a clear monotonic trend and fluctuate significantly, with the highest value near 30 GPa and the lowest near zero or negative. Positive and negative Cauchy pressure values in solid materials provide insights into their bonding type and structural stability. Generally, a positive Cauchy pressure correlates with stronger metallic adhesion, whereas a negative pressure indicates covalent adhesion. For $MgZn_2$, positive $C_{12} - C_{66}$ values indicate strong metallicity at the (001) surface, while the fluctuating $C_{13} - C_{44}$ on the (100) face suggests weaker metallicity at this surface.

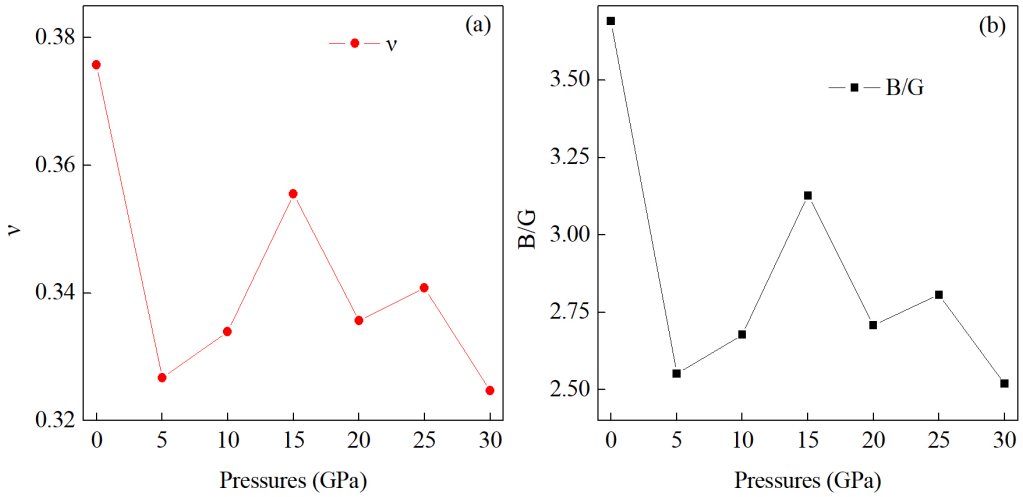


Figure 5. Variation in Poisson's ratio (ν) and modulus ratio (G/B) with pressure in $MgZn_2$, (**a**) is Poisson's ratio, (**b**) is modulus ratio.

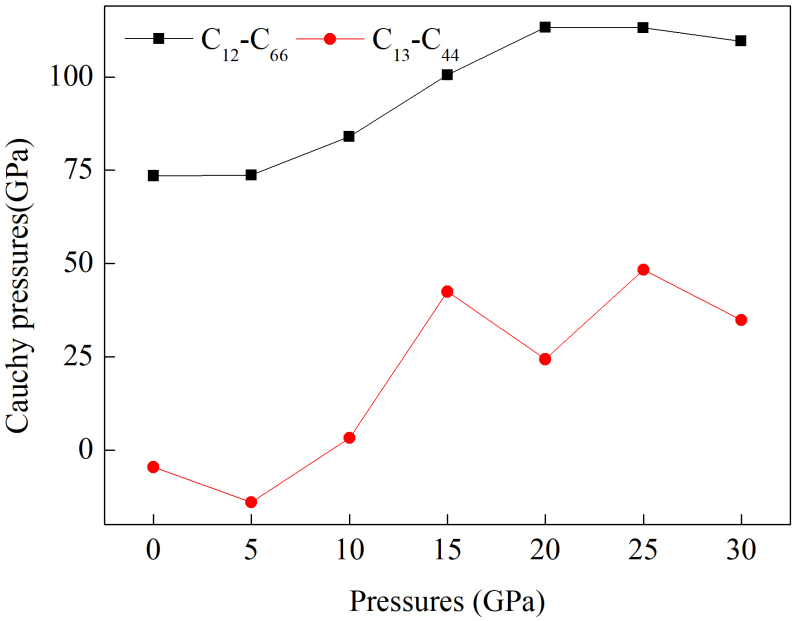


Figure 6. Cauchy pressure of $MgZn_2$ alloy under different pressures.

A key indicator of resistance to distortion, either plastic or elastic under the influence of external forces, is hardness. It is determined by such factors as the constants of elasticity, properties of plasticity, elongation, ductile properties and strength. In theory, polycrystalline hardness can be estimated using Equation (6) [41].

$$H = 2\left(\frac{G^3}{B^2}\right)^{0.585} - 3 \quad (6)$$

Figure 7 demonstrates the variation in hardness of $MgZn_2$ at different pressures. Overall, the hardness gradually increases with pressure increases ranging from 0 to 30 GPa.

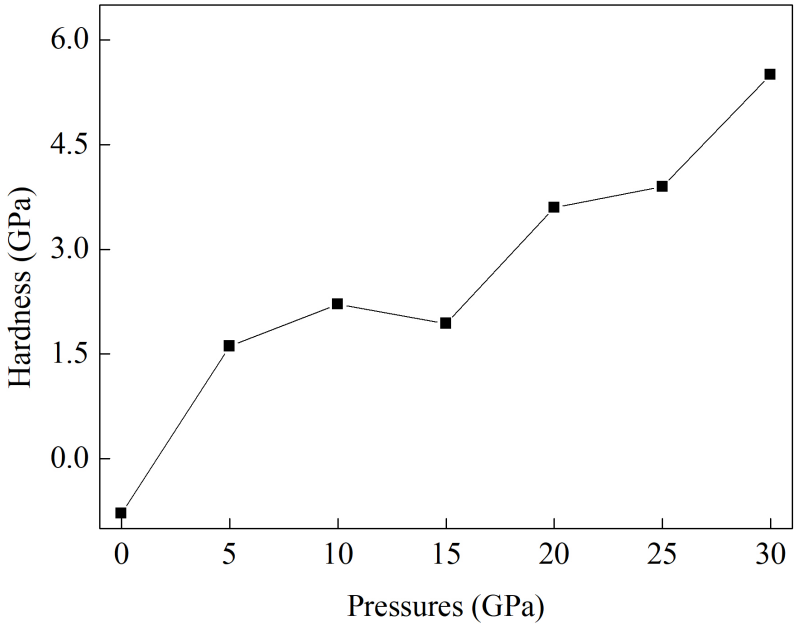


Figure 7. Hardness of $MgZn_2$ alloys under various pressures.

3.4. Pressure Elastic Anisotropy

Elastic anisotropy refers to the varying physical properties of a material depending on its orientation, and most materials exhibit this behavior. In intermetallic compounds, the study of elastic anisotropy closely relates to microcrack formation. The elastically anisotropic factor measures the resistance of a material to shear distortion in different directions, reflecting how shear energy changes with the orientation. The shear anisotropy factors are defined as follows: $A_{\{100\}}$ represents the shear resistance in the (100) shear plane between the <011> and <010> directions; $A_{\{010\}}$ describes the shear resistance direction between the axes <101> and <001> in the (010) shear plane; and $A_{\{001\}}$ characterizes the shear resistance between the directions <110> and <010> in the (001) shear plane. $A_{\{100\}}$, $A_{\{010\}}$ and $A_{\{001\}}$ are all one for a material with isotropic properties. A material's degree of anisotropy is given by any deviation from this value.

Using the obtained elastic constants, we calculated elastic anisotropy factors. The anisotropy factors are expressed in Equation (7) [42].

$$A_{\{100\}} = \frac{4C_{44}}{C_{11} + C_{33} - 2C_{13}}, \quad A_{\{010\}} = \frac{4C_{55}}{C_{22} + C_{33} - 2C_{23}}, \quad A_{\{001\}} = \frac{4C_{66}}{C_{11} + C_{22} - 2C_{12}} \tag{7}$$

The calculated anisotropy factors $A_{\{010\}}$, $A_{\{100\}}$ and $A_{\{001\}}$ for $MgZn_2$ subject to different types of pressure are shown in Figure 8a. It can be seen that $A_{\{100\}}$ and $A_{\{010\}}$ are significantly under one and increase with the pressure. In contrast, $A_{\{001\}}$ keeps a constant value of one for all pressure conditions. These results indicate that the anisotropy on planes 100 and 010 decreases as the pressure increases, while the 001 plane maintains its isotropic behavior. Since $MgZn_2$ is a hexagonal crystal, the 100 and 010 planes have lower symmetry, leading to stronger anisotropy on these planes. In contrast, the 001 plane has greater symmetry, leading to elastic isotropic properties for this plane. The compression anisotropic coefficient A^B and the shear anisotropic coefficient A^G are calculated using Equation (8) [43].

$$A^B = \frac{B_V - B_R}{B_V + B_R} \times 100\%, \quad A^G = \frac{G_V - G_R}{G_V + G_R} \times 100\% \tag{8}$$

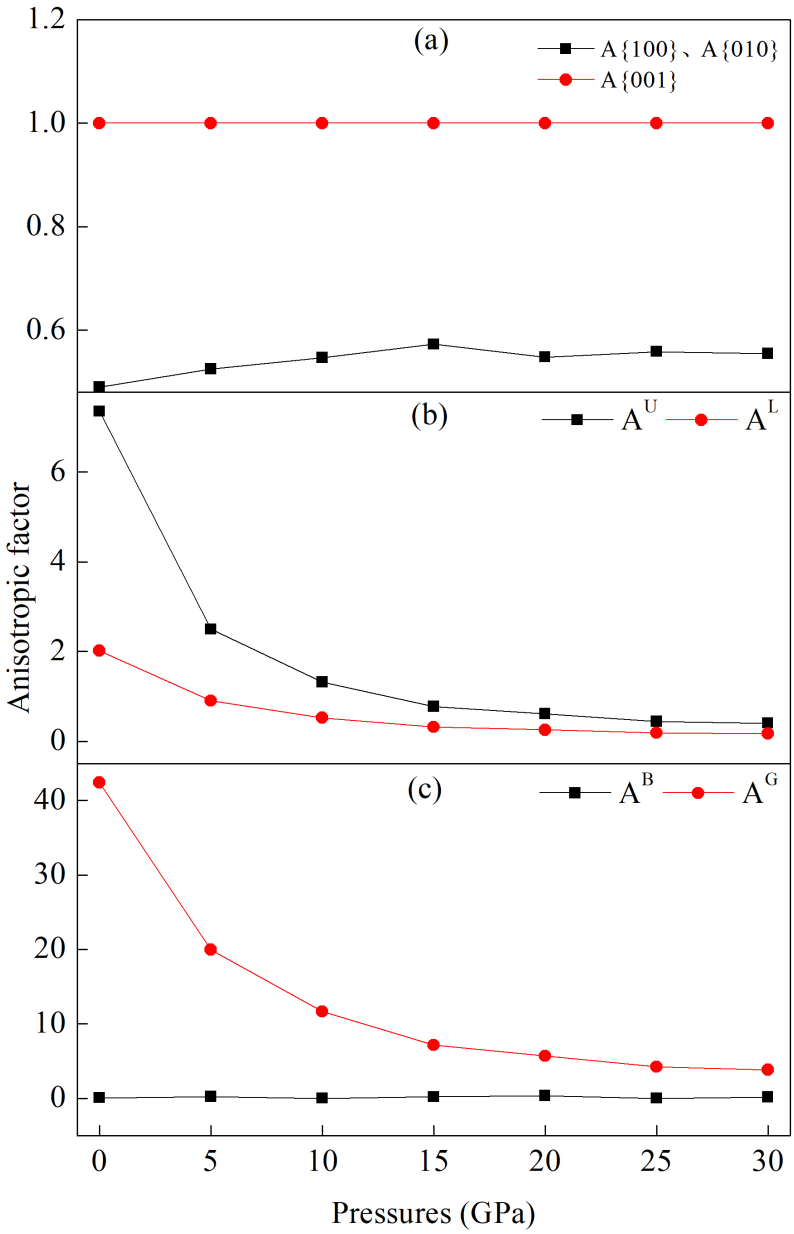


Figure 8. (**a**) $A_{\{100\}}$, $A_{\{010\}}$ and $A_{\{001\}}$ anisotropy factors; (**b**) broad spectrum index of anisotropy A^U and log Euclidean index of anisotropy A^L; and (**c**) percentage of compressive anisotropy A^B and percentage of shear anisotropy A^G for $MgZn_2$ at different pressures.

The broad spectrum factor of anisotropy A^U can be calculated using Equation (9) [44].

$$A^U = \frac{B_V}{B_R} + 5\frac{G_V}{G_R} - 6 \tag{9}$$

The logarithmic Euclidean scalar index of anisotropy (A^L) is calculated in Equation (10) [45].

$$A^L = \sqrt{\left[\ln\left(\frac{B_V}{B_R}\right)\right]^2 + 5\left[\ln\left(\frac{G_V}{G_R}\right)\right]^2} \tag{10}$$

With anisotropic materials, A^B, A^G, A^U and A^L should equal zero, with any variation indicating an anomalous degree of anisotropy. Figure 8b shows the broad spectrum index of anisotropy A^U and the logarithmic Euclidean anisotropy index A^L as a function of the pressure. Both A^U and A^L decrease as the pressure increases, approaching zero at 30 GPa,

suggesting that $MgZn_2$ becomes progressively more isotropic under pressure. Figure 8c presents the results for A^B and A^G, where it is clear that A^B remains close to zero with minimal variation across the pressure range of 0 to 30 GPa. Meanwhile, A^G is reduced as the pressure increases, gradually approaching zero. These findings further confirm that the anisotropy of $MgZn_2$ diminishes significantly with pressure. At the same time, this decrease can also start with the composition and processing technology. Adjust the ratio of Mg and Zn to make it close to the isotropic structure, increase the Mg content to change the atomic arrangement and bond distribution, add rare earth elements to affect the crystal symmetry. In terms of processing technology, the use of thermal deformation processing, such as hot rolling and hot forging, and atomic rearrangement, such as grain orientation randomization, the use of weaving control technology and the cross-rolling regulation of crystal weaving, can ensure that the different directions of the orientation result in a more uniform distribution to reduce the difference in performance and reduce anisotropy.

3.5. Speed of Sound Under Pressure

The longitudinal (V_l) and transverse (V_t) sound velocities of hexagonal $MgZn_2$ in the [100] and [001] directions can be obtained using the obtained C_{ij}, following Brugger's method. The sound speed in the [100] direction is given by Equation (11) [46,47].

$$[100]v_l = \sqrt{\frac{C_{11} - C_{12}}{2\rho}}, \quad [010]v_{t1} = \sqrt{\frac{C_{11}}{\rho}}, \quad [001]v_{t2} = \sqrt{\frac{C_{44}}{\rho}} \tag{11}$$

And the velocity of sound in direction [001] is computed as in Equation (12) [47,48].

$$[001]v_l = \sqrt{\frac{C_{33}}{\rho}}, \quad [100]v_{t1} = [010]v_{t2} = \sqrt{\frac{C_{44}}{\rho}} \tag{12}$$

with v_{t1} and v_{t2} corresponding to the transversal first and second modes, respectively, and ρ representing the density of the compound. As sound velocities depend on constants of elasticity, their anisotropy reflects the elastic anisotropy of $MgZn_2$. In addition, the velocity of sound in the longitudinal (V_L) and transverse (V_T) directions of $MgZn_2$ can be calculated using the resulting bulk modulus (B) and shear modulus (G), as shown in Equation (13) [48].

$$V_L = \sqrt{\frac{3B + 4G}{3\rho}}, \quad V_T = \sqrt{\frac{G}{\rho}} \tag{13}$$

Further, we can calculate the average velocity of sound according to Equation (14) [49].

$$V_M = \left[\frac{1}{3}\left(\frac{1}{V_L^3} + \frac{2}{V_T^3}\right)\right]^{-\frac{1}{3}} \tag{14}$$

The variation in sound velocities in $MgZn_2$ under different pressures (0–30 GPa), categorized by the propagation direction and wave type, is shown in Figure 9. Overall, all the sound velocities increase with the pressure. In Figure 9a, the longitudinal velocity of sound (v_l) in direction [100], as well as the velocities of the transverse waves (V_{t1} and V_{t2}) in the [010] and [001] axes, respectively, gradually increase with the pressure. Figure 9b shows a notable increase in the velocity of longitudinal sound (v_l) in direction [001], while the velocities (V_{t1} and V_{t2}) in the [100] and [010] orientations also show a slight increase with the pressure. In Figure 9c, the longitudinal average velocity of sound (V_L), average transverse velocity (V_T) and average total velocity (V_M) all increase with the pressure. Overall, these results indicate that $MgZn_2$'s ability to propagate acoustic waves improves with increasing pressure, suggesting the enhanced rigidity and density of the material under high-pressure conditions.

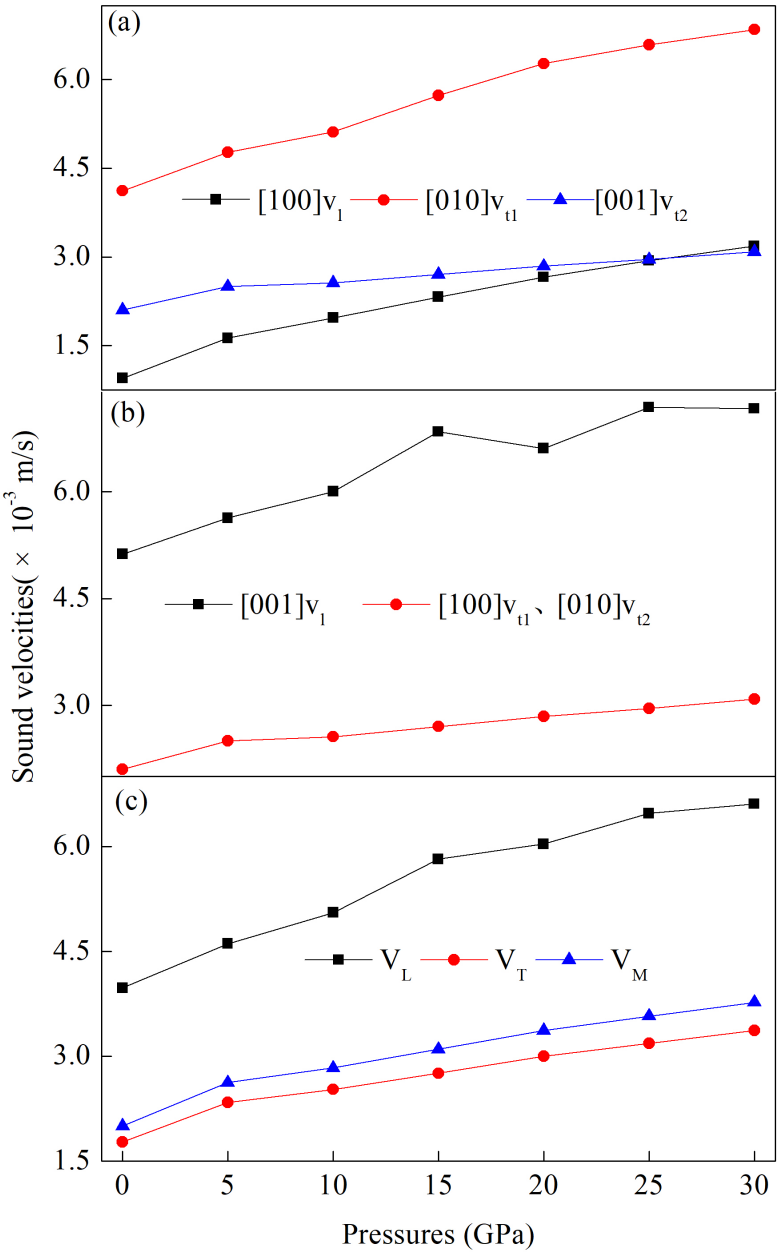


Figure 9. (**a**) Sound velocities in longitudinal (v_l) and transverse (v_{t1},v_{t2}) directions in [100] direction of $MgZn_2$ under varying pressures; (**b**) velocities of sound in longitudinal (v_l) and transverse (v_{t1}, v_{t2}) directions in [001] direction of $MgZn_2$ for varying pressures; and (**c**) sound velocity in longitudinal direction (V_L), sound velocity in transverse direction (V_T) and average sound velocity (V_M) of $MgZn_2$ crystal at different pressures.

4. Conclusions

First principle calculations applied to the research of materials under pressure are able to accurately reveal the evolution of the microstructure of materials in high-pressure environments, the changing law of mechanical properties and the response mechanism of physicochemical properties from the atomic and electronic levels based on the basic principles of quantum mechanics, without relying on the empirical speculation of experimental data, and provide an in-depth, accurate and prospective theoretical basis for the understanding of high-pressure behaviors in materials. This investigation systematically examined the mechanical and elastic characteristics of $MgZn_2$ alloys under varying pressures using first principle calculations, filling a gap in this area of previous research. The results show that lattice parameters (a/a_0, c/c_0) as well as the ratio of volumes (V/V_0) gradually

decrease with pressure increases. With the exception of the elastic constant C_{13}, all other constants of elasticity show significant increases with increasing pressure. $MgZn_2$ satisfies the mechanical stability criterion across a pressure range from 0 to 30 GPa, confirming stability within this interval. Furthermore, the ratio of Poisson remains consistently above 0.26, indicating good ductility, which aligns with the ratio of the bulk to shear modulus (B/G). Both the hardness and sound velocity of $MgZn_2$ increase with the pressure, while the degree of anisotropy decreases progressively. This investigation gives us important knowledge about the mechanical behavior of $MgZn_2$ under pressure, offering crucial guidance for applying and optimizing its properties in various fields. The mechanical response of $MgZn_2$ under higher pressure ranges or more complex pressure loading paths can be further investigated to explore whether there are new phase transitions or performance mutation points, which will help us to grasp its high-pressure behavioral properties in a more comprehensive way and provide more accurate data support for extreme high-pressure engineering applications.

Author Contributions: Conceptualization, C.X. and D.W.; methodology, X.Z.; software, Z.L. and Y.Z.; validation, Y.Z. and Z.C.; formal analysis, X.Z.; investigation, C.X.; resources, D.W.; data curation, D.W.; writing—original draft preparation, B.Y.; writing—review and editing, X.Z.; visualization, C.X.; supervision, C.X.; project administration, Y.Z.; funding acquisition, Z.L. and X.Z. All authors have read and agreed to the published version of this manuscript.

Funding: This research was funded by the Natural Science Foundation of Jiangxi Province (Grant No. 20242BAB25032), the Science and Technology Program of the Education Office of Jiangxi Province (Grant No. GJJ2401520), the PhD Start-up Fund of the Natural Science Foundation of Jinggangshan University (Grant JZB2329) and the Guiding Projects of Science and Technology Programme in Ji'an City, Jiangxi Province (Grant Nos. 20244-029653, 20244-029657).

Data Availability Statement: The raw data supporting the conclusions of this article will be made available by the authors on request.

Conflicts of Interest: The authors declare no conflicts of interest.

References

1. Mang, F.; Liu, J.; Zhu, Y.X.; Zhou, M.R.; Chen, G.J.; Shi, Q.Y. Microstructure and Corrosion Resistance of Modified Mg-$_5$Zn Alloy via Friction Stir Processing. *Acta Metall. Sin.* **2023**, 00281.
2. Alruqi, A.B. Tailoring the Mechanical Properties of X–C–Si (X= Al, Mg) Alloys for Aerospace and Automotive Industries: An ab Initio Study. *Sci. Adv. Mater.* **2024**, *16*, 224–230. [CrossRef]
3. Bai, J.; Yang, Y.; Wen, C.; Chen, J.; Zhou, G.; Jiang, B.; Peng, X.; Pan, F. Applications of magnesium alloys for aerospace: A review. *J. Magnes. Alloy.* **2023**, *11*, 3609–3619. [CrossRef]
4. Rafiei, S.; Habibolahzadeh, A.; Wiese, B. Environment-COnscious Magnesium (ECO-Mg): A Review. *Clean. Mater.* **2024**, *11*, 100230. [CrossRef]
5. Gupta, M. Feature Papers in Metal Matrix Composites. *Metals* **2024**, *14*, 1056. [CrossRef]
6. Çam, G.; Günen, A. Challenges and opportunities in the production of magnesium parts by directed energy deposition processes. *J. Magnes. Alloy.* **2024**, *12*, 1663–1686. [CrossRef]
7. Aziz, A.A.; Mamat, M.S.; Kechik, M.M.A.; Chan, K.F.; Muktar, M.I.; Tahir, N.A.M.; Kamis, S.L.; Yaakob, Y. Effect of anodizing voltage on surface and physical properties of CNTs incorporated aluminium oxide films. *J. Tribol.* **2024**, *41*, 144–161.
8. Lipińska, M.; Kooijman, A.; Śnieżek, L.; Szachogłuchowicz, I.; Torzewski, J.; Gonzalez-Garcia, Y.; Lewandowska, M. The Influence of Microstructure Evolution on the Mechanical and Electrochemical Properties of Dissimilar Welds from Aluminum Alloys Manufactured Via Friction Stir Welding. *Metall. Mater. Trans. A* **2024**, *55*, 4373–4390. [CrossRef]
9. Yin, H.; Wen, K.; Li, Z.; Li, X.; Li, Y.; Yan, L.; Yan, H.; Yu, M.; Zhang, Y.; Xiong, B. Effect of Zn/Mg ratio on the microstructure and mechanical properties of as-cast Al–Zn–Mg–Cu alloys and the phase transformation during homogenization. *J. Mater. Res. Technol.* **2023**, *26*, 3646–3660. [CrossRef]
10. Koltygina, T.; Bazhenov, V.; Koltygin, A.; Prosviryakov, A.; Tabachkova, N.; Baranov, I.; Komissarov, A.; Bazlov, A. Microstructure and mechanical properties of new Mg–Zn–Y–Zr alloys with high castability and ignition resistance. *Int. J. Miner. Metall. Mater.* **2024**, *31*, 1–13. [CrossRef]
11. Xie, Y.P.; Wang, Z.Y.; Hou, Z. The phase stability and elastic properties of $MgZn_2$ and Mg_4Zn_7 in Mg–Zn alloys. *Scr. Mater.* **2013**, *68*, 495–498. [CrossRef]
12. Byun, J.M.; Yu, J.M.; Kim, D.K.; Kim, T.Y.; Jung, W.S.; Kim, Y.D. Corrosion behavior of Mg_2Zn_{11} and $MgZn_2$ single phases. *J. Korean Inst. Met. Mater.* **2013**, *51*, 413–419. [CrossRef]

13. Shi, Y.; Liu, X.Q.; Liu, Z.L.; Xie, H.J.; Wang, Y.H.; Li, J. Effect of Zn content on corrosion behavior of Mg-Y-Zn alloys. *J. Min. Metall. Sect. B Metall.* **2022**, *58*, 51–61. [CrossRef]
14. Andrae, D.; Paulus, B.; Wedig, U.; Jansen, M. A First-Principles Study of Electronic Structure of the Laves Phase $MgZn_2$. *Z. Anorg. Allg. Chem.* **2013**, *639*, 1963–1967. [CrossRef]
15. Wu, M.M.; Wen, L.; Tang, B.Y.; Peng, L.M.; Ding, W.J. First-principles study of elastic and electronic properties of $MgZn_2$ and $ScZn_2$ phases in Mg–Sc–Zn alloy. *J. Alloy. Compd.* **2010**, *506*, 412–417. [CrossRef]
16. Perdew, J.P.; Burke, K.; Ernzerhof, M. Generalized gradient approximation made simple. *Phys. Rev. Lett.* **1996**, *77*, 3865. [CrossRef] [PubMed]
17. Hohenberg, P.; Kohn, W. Inhomogeneous electron gas. *Phys. Rev.* **1964**, *136*, B864. [CrossRef]
18. Kohn, W.; Sham, L.J. Self-consistent equations including exchange and correlation effects. *Phys. Rev.* **1965**, *140*, A1133. [CrossRef]
19. Milman, V.; Winkler, B.; White, J.; Pickard, C.; Payne, M.; Akhmatskaya, E.; Nobes, R. Electronic structure, properties, and phase stability of inorganic crystals: A pseudopotential plane-wave study. *Int. J. Quantum Chem.* **2000**, *77*, 895–910. [CrossRef]
20. Segall, M.; Lindan, P.J.; Probert, M.A.; Pickard, C.J.; Hasnip, P.J.; Clark, S.; Payne, M. First-principles simulation: Ideas, illustrations and the CASTEP code. *J. Phys. Condens. Matter* **2002**, *14*, 2717. [CrossRef]
21. Clark, S.J.; Segall, M.D.; Pickard, C.J.; Hasnip, P.J.; Probert, M.I.; Refson, K.; Payne, M.C. First principles methods using CASTEP. *Z. Krist.-Cryst. Mater.* **2005**, *220*, 567–570. [CrossRef]
22. Mull, T.; Baumeister, B.; Menges, M.; Freund, H.J.; Weide, D.; Fischer, C.; Andresen, P. Bimodal velocity distributions after ultraviolet-laser-induced desorption of NO from oxide surfaces. Experiments and results of model calculations. *J. Chem. Phys.* **1992**, *96*, 7108–7116. [CrossRef]
23. Hamann, D. Optimized norm-conserving Vanderbilt pseudopotentials. *Phys. Rev. B Condens. Matter Mater. Phys.* **2013**, *88*, 085117. [CrossRef]
24. Monkhorst, H.J.; Pack, J.D. Special points for Brillouin-zone integrations. *Phys. Rev. B* **1976**, *13*, 5188. [CrossRef]
25. Stein, F.; Leineweber, A. Laves phases: A review of their functional and structural applications and an improved fundamental understanding of stability and properties. *J. Mater. Sci.* **2021**, *56*, 5321–5427.
26. Cazorla, C.; Errandonea, D.; Sola, E. High-pressure phases, vibrational properties, and electronic structure of $Ne(He)_2$ and $Ar(He)_2$: A first-principles study. *Phys. Rev. Condens. Matter Mater. Phys.* **2009**, *80*, 064105. [CrossRef]
27. Le Page, Y.; Saxe, P. Symmetry-general least-squares extraction of elastic data for strained materials from ab initio calculations of stress. *Phys. Rev. B* **2002**, *65*, 104104. [CrossRef]
28. Ohba, T.; Kitano, Y.; Komura, Y. The charge-density study of the Laves phases, $MgZn_2$ and $MgCu_2$. *Acta Crystallogr. Sect. C Cryst. Struct. Commun.* **1984**, *40*, 1–5. [CrossRef]
29. Mao, P.; Yu, B.; Liu, Z.; Wang, F.; Ju, Y. First-principles calculations of structural, elastic and electronic properties of AB_2 type intermetallics in Mg–Zn–Ca–Cu alloy. *J. Magnes. Alloy.* **2013**, *1*, 256–262. [CrossRef]
30. Zheng, B.; Zhao, L.; Hu, X.; Dong, S.; Li, H. First-principles studies of $Mg_{17}Al_{12}$, Mg_2Al_3, Mg_2Sn, $MgZn_2$, Mg_2Ni and Al_3Ni phases. *Phys. B Condens. Matter* **2019**, *560*, 255–260. [CrossRef]
31. Angel, R.J.; Alvaro, M.; Gonzalez-Platas, J. EosFit7c and a Fortran module (library) for equation of state calculations. *Z. Krist.-Cryst. Mater.* **2014**, *229*, 405–419. [CrossRef]
32. Birch, F. Finite elastic strain of cubic crystals. *Phys. Rev.* **1947**, *71*, 809–824. [CrossRef]
33. Zeng, X.; Peng, R.; Yu, Y.; Hu, Z.; Wen, Y.; Song, L. Pressure effect on elastic constants and related properties of Ti_3Al intermetallic compound: A first-principles study. *Materials* **2018**, *11*, 2015. [CrossRef] [PubMed]
34. Sin'Ko, G.; Smirnov, N. Ab initio calculations of elastic constants and thermodynamic properties of bcc, fcc, and hcp Al crystals under pressure. *J. Phys. Condens. Matter* **2002**, *14*, 6989.
35. Cheng, H.C.; Yu, C.F.; Chen, W.H. First-principles density functional calculation of mechanical, thermodynamic and electronic properties of CuIn and Cu2In crystals. *J. Alloy. Compd.* **2013**, *546*, 286–295. [CrossRef]
36. Waqdim, A.; Agouri, M.; Ouali, M.; Taj, S.; Manaut, B.; El Idrissi, M. Ab initio insight into the physical properties of new ferroelectric perovskite oxide materials $XGeO_3$ (X= Sr, Ca). *Rev. Mex. Física* **2024**, *70*, 051603-1. [CrossRef]
37. Reuss, A. Calculation of the flow limits of mixed crystals on the basis of the plasticity of monocrystals. *Z. Angew. Math. Mech* **1929**, *9*, 49–58. [CrossRef]
38. Frantsevich, I.N. *Elastic Constants and Elastic Moduli of Metals and Insulators*; Naukova Dumka: Kyiv, Ukraine, 1982.
39. Pugh, S. XCII. Relations between the elastic moduli and the plastic properties of polycrystalline pure metals. *London Edinburgh Dublin Philos. Mag. J. Sci.* **1954**, *45*, 823–843. [CrossRef]
40. Pettifor, D. Theoretical predictions of structure and related properties of intermetallics. *Mater. Sci. Technol.* **1992**, *8*, 345–349. [CrossRef]
41. Chen, X.Q.; Niu, H.; Li, D.; Li, Y. Modeling hardness of polycrystalline materials and bulk metallic glasses. *Intermetallics* **2011**, *19*, 1275–1281. [CrossRef]
42. Mao, P.; Yu, B.; Liu, Z.; Wang, F.; Ju, Y. First-principles investigation on mechanical, electronic, and thermodynamic properties of Mg_2Sr under high pressure. *J. Appl. Phys.* **2015**, *117*, 115903. [CrossRef]
43. Chung, D.; Buessem, W. The elastic anisotropy of crystals. *J. Appl. Phys.* **1967**, *38*, 2010–2012. [CrossRef]
44. Ranganathan, S.I.; Ostoja-Starzewski, M. Universal elastic anisotropy index. *Phys. Rev. Lett.* **2008**, *101*, 055504. [CrossRef] [PubMed]

45. Kube, C.M. Elastic anisotropy of crystals. *AIP Adv.* **2016**, *6*, 095209. [CrossRef]
46. Duan, Y.; Sun, Y.; Peng, M.; Zhou, S. Anisotropic elastic properties of the Ca–Pb compounds. *J. Alloy. Compd.* **2014**, *595*, 14–21. [CrossRef]
47. Sun, L.; Gao, Y.; Xiao, B.; Li, Y.; Wang, G. Anisotropic elastic and thermal properties of titanium borides by first-principles calculations. *J. Alloy. Compd.* **2013**, *579*, 457–467. [CrossRef]
48. Schneider, E.; Anderson, O.; Soga, N. *Elastic Constants and Their Measurement*; McGraw-Hill: New York, NY, USA, 1974.
49. Anderson, O.L. A simplified method for calculating the Debye temperature from elastic constants. *J. Phys. Chem. Solids* **1963**, *24*, 909–917. [CrossRef]

Disclaimer/Publisher's Note: The statements, opinions and data contained in all publications are solely those of the individual author(s) and contributor(s) and not of MDPI and/or the editor(s). MDPI and/or the editor(s) disclaim responsibility for any injury to people or property resulting from any ideas, methods, instructions or products referred to in the content.